# LANGMUIR

Article pubs.acs.org/Langmuir

# Electronic and Optical Property Control of Polycation/MXene Layerby-Layer Assemblies with Chemically Diverse MXenes

Ian J. Echols, Hyosung An, Junyeong Yun, Kasturi T. Sarang, Ju-Hyun Oh, Touseef Habib, Xiaofei Zhao, Huaixuan Cao, Dustin E. Holta, Miladin Radovic, Micah J. Green, and Jodie L. Lutkenhaus\*



Cite This: Langmuir 2021, 37, 11338-11350



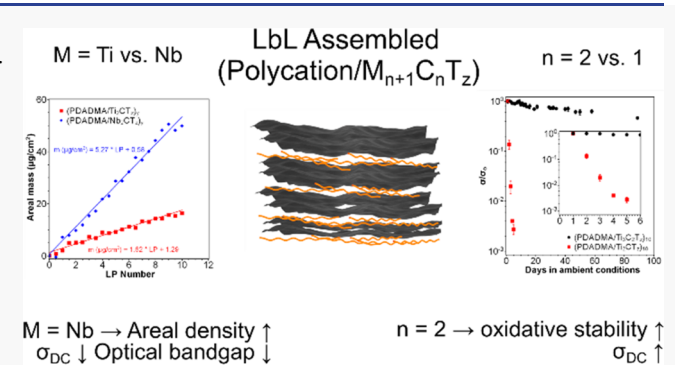
**ACCESS** I

III Metrics & More

Article Recommendations

Supporting Information

ABSTRACT: MXenes, 2D nanomaterials derived from ceramic MAX phases, have drawn considerable interest in a wide variety of fields including energy storage, catalysis, and sensing. There are many possible MXene compositions due to the chemical and structural diversity of parent MAX phases, which can bear different possible metal atoms "M", number of layers, and carbon or nitrogen "X" constituents. Despite the potential variety in MXene types, the bulk of MXene research focuses upon the first MXene discovered, Ti<sub>3</sub>C<sub>2</sub>T. With the recent discovery of polymer/MXene multilayer assemblies as thin films and coatings, there is a need to broaden the accessible types of multilayers by including MXenes other than Ti<sub>3</sub>C<sub>2</sub>T<sub>2</sub>; however, it is not clear how altering the MXene type influences the resulting multilayer growth and



properties. Here, we report on the first use of MXenes other than Ti<sub>3</sub>C<sub>2</sub>T<sub>2</sub>, specifically Ti<sub>2</sub>CT<sub>2</sub> and Nb<sub>2</sub>CT<sub>2</sub>, for the layer-bylayer (LbL) assembly of polycation/MXene multilayers. By comparing these MXenes, we evaluate both how changing M (Ti vs Nb) and "n" (Ti<sub>3</sub>C<sub>7</sub>T<sub>e</sub>vs Ti<sub>2</sub>CT<sub>e</sub>) affect the growth and properties of the resulting multilayer. Specifically, the aqueous LbL assembly of each MXene with poly(diallyldimethylammonium) into films and coatings is examined. Further, we compare the oxidative stability, optoelectronic properties (refractive index, absorption coefficient, optical conductivity, and direct and indirect optical band gaps), and the radio frequency heating response of each multilayer. We observe that MXene multilayers with higher "n" are more electrically conductive and oxidatively stable. We also demonstrate that Nb<sub>2</sub>CT<sub>z</sub> containing films have lower optical band gaps and refractive indices at the cost of lower electrical conductivities as compared to their Ti<sub>2</sub>CT<sub>z</sub> counterparts. Our work demonstrates that the properties of MXene/polycation multilayers are highly dependent on the choice of constituent MXene and that the MXene type can be altered to suit specific applications.

#### INTRODUCTION

Layer-by-layer (LbL) assembly is a highly versatile method for fabricating thin films with discrete and alternating layers. This method relies on the electrostatic attraction between two oppositely charged materials and the entropic release of counterions. This fabrication method also allows for ultrathin and conformal coatings on a variety of substrates (e.g., tubes, plastic, glass, fabric, etc.).2 Additionally, the process is highly tunable as both thickness and composition can be changed by varying the constituent materials, layer pair number, pH and concentration of the assembly baths, deposition time, and the rinse and drying procedures. Recently, this process has been used to make LbL MXene multilayers due to the highly negative ζ-potential of the MXene nanosheets.<sup>3</sup> These multilayers have been used for a number of applications (e.g., sensing, energy storage, catalysis, and electromagnetic interference (EMI) shielding) and have demonstrated improved surface adhesion as compared to drop-cast MXene films. 2,4-10 However, only Ti<sub>3</sub>C<sub>2</sub>T<sub>z</sub> MXene nanosheets have

been used to assemble LbL films to date, presenting an opportunity to broaden the range of accessible MXene multilayers.

MXenes, represented with the chemical formula  $M_{n+1}X_nT_z$ where M is a transition metal, X is either carbon or nitrogen, T is a surface terminal group (oxygen, fluoride, or hydroxyl), and n is 1, 2, or 3, are a class of 2D nanomaterials known for their graphene-like structure, high electrical conductivities, and wide array of possible compositions. 11,12 Since their discovery, they have drawn interest for a variety of applications due to their favorable properties (e.g., high conductivity, abundant surface functional groups, high aspect ratios, etc.). 2,13-15 The most

Received: July 19, 2021 Published: September 15, 2021





commonly used MXene to date is  $Ti_3C_2T_z$  and has been the focus of the bulk of MXene studies. However, a wide variety of other MXenes have also been theoretically reported, and a growing number of those have been successfully synthesized. <sup>14,16</sup> Despite this, these new MXenes have yet to be explored as materials for LbL assembly.

More recently, newer MXenes, such as Ti<sub>2</sub>CT<sub>z</sub> and Nb<sub>2</sub>CT<sub>z</sub>, have been successfully synthesized and studied. <sup>17,18</sup> As the starting MAX phase used to produce the MXene changes, the properties of the resultant MXene change as well. For example, theoretical comparisons of Ti-based MXenes with varying "n" predict that the Fermi level increases with increasing n, indicating improved electrical properties. <sup>19</sup> In the case of Nb-based MXenes, the conductivity has been predicted to be orders of magnitude lower than that of Ti-based MXenes for the same "n" and resistivity was inversely related to temperature, in contrast to the metal-like behavior of Ti-based MXenes. <sup>14,17</sup> Despite the stark difference in properties of the different MXenes, no studies to date have explored the effect of different MXene compositions on the properties of MXene-based multilayer composites.

Here, we report the assembly of (polymer/MXene) multilayers using different dispersions of single- or few-layered MXenes (Ti<sub>3</sub>C<sub>2</sub>T<sub>z</sub>, Ti<sub>2</sub>CT<sub>z</sub>, and Nb<sub>2</sub>CT<sub>z</sub>) via a layer-by-layer (LbL) assembly method. To our knowledge, this is the first report of the use of Ti<sub>2</sub>CT<sub>z</sub> and Nb<sub>2</sub>CT<sub>z</sub> in LbL-assembled thin films. We compare the effect of varying "n" and "M" of the constituent MXene on the layer growth profiles of the thin films by profilometry, ellipsometry, and UV-vis spectroscopy. After fabricating the multilayers, we compared their electrical and optical properties to further show the effects of varying "n" and "M" of the constituent MXene. Based on theoretical reports and previous experimental results with pure MXene films, we expect that MXenes with M = Ti and larger n will demonstrate improved electrical properties. 14,17,19 Finally, we compare the oxidative stability of the thin films and their heating responses to RF fields. Taken together, these results broaden the number of accessible polymer/MXene multilayers and provide a path forward for tuning electrical and optical properties of the resultant coatings.

## **■ EXPERIMENTAL SECTION**

Materials. Poly(diallyldimethyl ammonium chloride) (PDADMA, MW = 200,000 to 350,000 g/mol, 20 wt % in water), L-ascorbic acid (AA, 99%), dimethyl sulfoxide (DMSO, ReagentPlus, >99.5%), and ammonium hydroxide (28% in water) were purchased from Sigma-Aldrich. Titanium (Ti, -325 mesh, 99%), aluminum (Al, -325 mesh, 99.5%), niobium (Nb, -325 mesh, 99.8%), TiC (2-3 micrometer, 99.5%), hydrofluoric acid (HF, 48-51%), and lithium fluoride (LiF, >98%) were purchased from Alfa Aesar. Hydrogen peroxide (H<sub>2</sub>O<sub>2</sub>) 30%) was purchased from BDH. Isopropyl alcohol (IPA, 99%), acetone (>99.55), and slide glass (75  $\times$  25  $\times$  1 mm) were purchased from VWR. Ti/Au quartz crystal substrates (5 MHz) were purchased from Inficon. Si wafers were obtained from University Wafer. Melinex ST505 (polyethylene terephthalate (PET) substrates, 0.2 mm thickness) was purchased from Tekra. A Milli-Q integral water purification system for ultrapure water was used to obtain 18.2  $M\Omega$ cm (Milli-Q) water. All materials were used as received.

**MAX Phase Synthesis.** MAX phase powders were prepared by pressureless sintering following a previous report. <sup>20</sup> A molar ratio of Ti:Al:C = 3:1.2:1.95 was used to make Ti<sub>3</sub>AlC<sub>2</sub> from titanium, aluminum, and TiC starting powders. Powders were ball milled for 12 h in 50 mL centrifuge vials with 35 mm high-density ZrO<sub>2</sub> cylinders (Glenn Mills Inc.). The milled elemental powders were placed in a 50 mm alumina tube furnace (MTI Corporation, GSL-1600X-50-UL).

Oxygen and other reactive gases were removed from the furnace by three argon purges. After returning to atmospheric pressure under argon flow, the tube was heated at a rate of  $10\,^{\circ}\mathrm{C}$  per minute to 1510  $^{\circ}\mathrm{C}$  and sintered for 4 h. The resultant MAX phase was allowed to cool naturally to room temperature and subsequently ground using a mortar and pestle and sieved into particles in the range of  $20-45\,$  micrometers.

 $Nb_2AlC$  and  $Ti_2AlC$  were prepared following a similar procedure.  $Nb_2AlC$  was prepared using a molar ratio of Nb:Al:C=2:1.1:0.95 and sintered at  $1600\ ^{\circ}C$  for 4 h.  $Ti_2AlC$  was prepared using a molar ratio of Ti:Al:C=2:1.2:0.95 and sintered at  $1400\ ^{\circ}C$  for 4 h. The particle size range of  $Ti_2AlC$  was <20 micrometers.

MXene Clay Synthesis. MXene clay was obtained by the selective etching of the A phase from a MAX phase precursor. All etching was done in an HF-rated fume hood due to the hazardous nature of HF. Etching containers were made of polypropylene, and holes were drilled in the caps to prevent pressure build-up of the reaction vessel. Ti<sub>3</sub>C<sub>2</sub>T<sub>z</sub> clay was synthesized using HCl and LiF following previous reports. PHCl was diluted to 6 M with DI water, and 50 mL was added to the polypropylene etching container. LiF (3.3 g) was then added under constant stirring. After all the LiF dissolved, the mixture was heated to 40 °C. Ti<sub>3</sub>AlC<sub>2</sub> (5 g) was slowly added under constant stirring and allowed to etch for 45 h. The product was then washed until the pH of the mixture reached 6 by a centrifugal washing process (9000 RPM for 20 min). Ti<sub>2</sub>CT<sub>z</sub> clay was synthesized following a similar procedure to Ti<sub>3</sub>CT<sub>z</sub>, albeit with a reduced etching time of 12 h.<sup>20</sup>

Similar to previous reports,  $Nb_2CT_z$  clay was obtained by the selective etching of Al from the  $Nb_2AlC$  MAX phase using HF at room temperature. Nb<sub>2</sub>AlC (1 g, 20–45 micrometers) was slowly added to 10 mL of concentrated HF (48–51%) under constant stirring in a 100 mL polypropylene beaker with screw cap and left to etch for 90 h. After etching, residual HF was removed from the mixture by a centrifugal washing process (9000 RPM for 20 min) with DI water. Washing was repeated until the pH of the mixture was  $\sim$ 5.

**MXene Nanosheet Synthesis.** MXene nanosheets were obtained by the intercalation and delamination of MXene clay.  ${\rm Ti_3C_2T_z}$  clay was intercalated by dispersing the clay in 16.67 mL of DMSO per gram of the starting MAX phase. The dispersion was then left to stir continuously for 20 h at room temperature. DMSO was then removed by three cycles of centrifugal solvent exchange with DI water at 5000 RPM for 4 h. The intercalated clay was then bath sonicated for 1 h at room temperature to delaminate the  ${\rm Ti_3C_2T_z}$  clay. The delaminated nanosheet dispersion was obtained by centrifuging the bath-sonicated dispersion for 1 h at 3500 RPM and collecting the supernatant. Concentration was determined by vacuum filtration of a known volume of nanosheet dispersion. The same procedure was used for intercalation and delamination of  ${\rm Ti_2CT_z}$  clay to obtain  ${\rm Ti_2CT_z}$  nanosheets.

 ${
m Nb_2CT_z}$  clay was intercalated using 20 wt % TBAOH in DI water. Twenty-five milliliters of 20 wt % TBAOH per gram of the starting  ${
m Nb_2AlC}$  MAX phase was added to the clay. The suspension was constantly stirred for 8 h at room temperature. TBAOH was then removed by a solvent exchange process with DI water by centrifuging at 10,000 RPM for 20 min and decanting the supernatant. The solvent exchange process was carried out twice. The intercalated  ${
m Nb_2CT_z}$  suspension was then bath sonicated in an ice bath for 1 h and subsequently centrifuged at 3500 RPM for 30 min to collect the  ${
m Nb_2CT_z}$  nanosheets in the supernatant. The bath sonication and centrifugation process was repeated to improve the yield of the process, and both supernatants were combined. The resulting dispersion contained the  ${
m Nb_2CT_z}$  nanosheets. The concentration of the dispersion was determined by UV—vis spectrophotometry using an extinction coefficient of 1080 L/g/m at 776 nm.

Layer-by-Layer Assembly of Thin Films. After the synthesis of the MXenes, the resultant dispersions were diluted to 1 mg/mL. Due to the poor oxidative stability of MXenes, it is important to consider oxidation during LbL assembly. To mitigate oxidation during this process, an antioxidant (1 mg/mL AA) was added to all MXene, polycation, and water wash baths used for assembly.<sup>22</sup> MXene

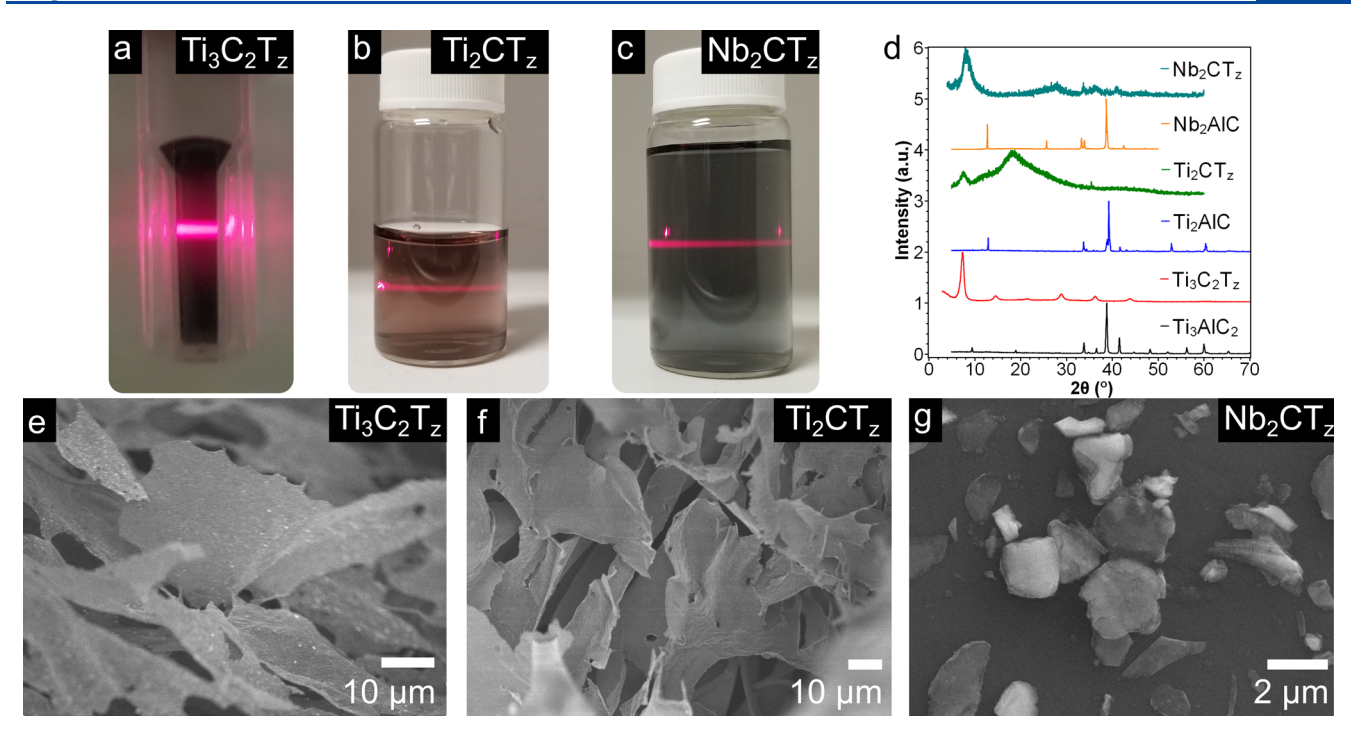


Figure 1. Colloidal dispersions ( $\sim$ 0.05 mg/mL) of (a) Ti<sub>3</sub>C<sub>2</sub>T<sub>z</sub>, (b) Ti<sub>2</sub>CT<sub>z</sub>, and (c) Nb<sub>2</sub>CT<sub>z</sub> displaying the Tyndall effect. (d) XRD peaks of Ti<sub>3</sub>C<sub>2</sub>T<sub>z</sub>, Ti<sub>2</sub>CT<sub>z</sub>, and Nb<sub>2</sub>CT<sub>z</sub> with respective MAX phase precursors. Top-down SEM images of (e) freeze-dried Ti<sub>3</sub>C<sub>2</sub>T<sub>z</sub>, (f) freeze-dried Ti<sub>2</sub>CT<sub>z</sub>, and (g) drop-cast Nb<sub>2</sub>CT<sub>z</sub>. Samples for XRD were prepared by VAF.

dispersions were diluted and used for assembly immediately after the concentration of the initial MXene dispersion was determined to minimize oxidation prior to LbL assembly. The pH of the MXene dispersions was not adjusted. Fabrication of (PDADMA/MXene), multilayers, where "y" represents the number of layer pairs (LP), on glass, Si, PET, and 5 MHz Ti/Au quartz crystal substrates following a previous report. Substrates were cleaned prior to use. Glass and Si wafers were bath sonicated in isopropyl alcohol (IPA) for 15 min and subsequently washed with water and acetone. PET substrates were bath sonicated in IPA for 15 min and subsequently washed with water. Quartz crystal substrates were plasma treated for 10 min then cleaned in a basic piranha solution (5:1:1 Milli-Q water:ammonium hydroxide:hydrogen peroxide) at 75 °C. After cleaning, substrates were then plasma treated for 3 min (10 min for quartz crystal substrates) to render the surface hydrophilic and negatively charged. Substrates were then submerged in 1 mg/mL PDADMA with 1 mg/ mL AA for 15 min. PDADMA was used at its natural pH (pH 7.8). The substrates were then washed in three separate Milli-Q water baths (each containing 1 mg/mL AA) for 1 min each and subsequently dried with compressed air to remove loosely adhered polymers and prevent aggregation. The substrates were then submerged in 1 mg/mL MXene dispersion with 1 mg/mL AA for 15 min and washed and dried following the same procedure as for the PDADMA layer. This constituted one LP and was repeated for the desired number of LPs. The deposition of a layer pair took approximately 1 h to complete. Samples were then stored under vacuum at room temperature to remove any excess interlayer water.

Characterization. To characterize the starting MXenes, X-ray powder diffraction (XRD, Bruker-AXS Advanced Bragg—Brentano X-ray powder diffractometer), scanning electron microscopy (SEM, JEOL JSM-7500F), X-ray photoelectron spectroscopy (XPS, Omicron XPS/UPS system with an Argus detector), dynamic light scattering (DLS, Malvern Zetasizer Nano ZS), and ζ-potential measurements (Malvern Zetasizer Nano ZS) were used. Samples for XRD and XPS were prepared by vacuum-assisted filtration (VAF). Samples for SEM were prepared by freeze drying for Ti<sub>3</sub>C<sub>2</sub>T<sub>z</sub> and Ti<sub>2</sub>CT<sub>z</sub> and by drop casting a dilute (~0.05 mg/mL) dispersion for Nb<sub>2</sub>CT<sub>z</sub>. Samples for DLS and ζ-potential measurements were prepared by diluting the asprepared MXene dispersions to ~0.05 mg/mL. Atomic force

microscopy (AFM, Bruker Dimension Icon AFM) and SEM were used to examine the surface morphology of the polycation/MXene multilayers. Samples were used as prepared on glass slides and PET for AFM and SEM, respectively. AFM topographic scans were also used to evaluate the degree of oxidation of the multilayers during the LbL assembly process by the presence of small oxides on the surface of the multilayers.

Profilometry, spectrophotometry, and quartz crystal microbalance (QCM) were utilized to monitor film growth. Profilometric thickness and root-mean-square (RMS) roughness  $(R_a)$  of thin films assembled on glass substrates were measured as a function of the LP number using a profilometer (KLA Tencor D-100). A UV-vis spectrophotometer (Shimadzu SolidSpec-3700 UV-vis-NIR) was used to measure absorbance of the films on glass substrates. Standard errors for the growth rates were calculated using a 95% confidence interval. Film composition was obtained by QCM (MAXTEK RQCM Research) for coatings on 5 MHz Ti/Au quartz crystal substrates. The frequency change was recorded after every half LP and converted into mass deposited using the Sauerbrey equation. A four-point probe (Lucas Labs S-302-4) was used to measure sheet resistance and calculate conductivity of films.  $\sigma_{\rm DC}$  as a function of the LP number was also used as a metric for evaluating the degree of oxidation of MXene during the assembly process, as oxidation would result in a decrease in conductivity. Absorbance and conductivity were measured over time to compare oxidative stability of films assembled using different MXenes. Films were stored under ambient conditions (~25 °C, ~45% RH) when monitoring how properties changed over time. The optical properties of note include refractive index, absorption coefficient, optical conductivity, and direct and indirect optical band gap. Refractive index was measured by ellipsometry (LSE Stokes Ellipsometer). The absorption coefficient ( $\alpha$ ) was taken at a wavelength of 550 nm, a common wavelength used to compare transparent, conductive films, and  $\alpha$  was calculated following the Beer-Lambert relation (eq 1):<sup>23,24</sup>

$$\alpha = 2.303 \frac{A}{t} \tag{1}$$

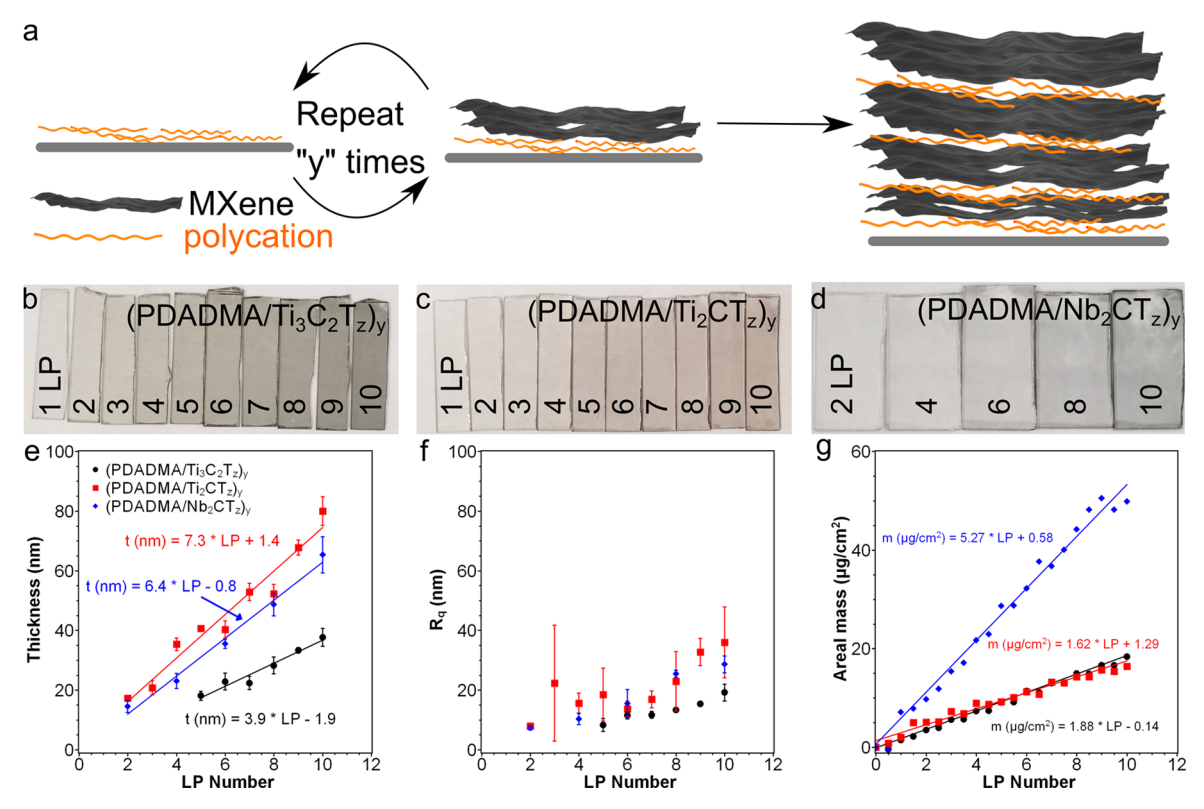


**Figure 2.** (a) Schematic of the LbL assembly process. Digital images of (b)  $(PDADMA/Ti_3C_2T_z)_y$ , (c)  $(PDADMA/Ti_2CT_z)_y$ , and (d)  $(PDADMA/Nb_2CT_z)_y$  multilayers. Profilometric (e) thickness and (f) roughness, as well as (g) areal mass of  $(PDADMA/MXene)_y$  multilayers as a function of the LP number. The legend in (e) also applies to panels (f) and (g).

where A is the absorbance and t is the thickness. The optical conductivity at 550 nm was calculated following previous reports as shown in eq 2:<sup>24</sup>

$$\sqrt{\frac{1}{\tau_{550}}} - 1 = \frac{Z_o}{2} \sigma_{op} t \tag{2}$$

where  $\tau_{\rm 550}$  is the transmittance at 550 nm,  $Z_{\rm o}$  is the impedance of free space (376.73  $\Omega$ ),  $\sigma_{\rm op}$  is the optical conductivity, and t is the thickness.

Optical band gaps were determined using Tauc plots in which  $(\alpha h v)^{1/n}$  is plotted as a function of the energy of the light, h v, where  $\alpha$  is the absorption coefficient, h is Planck's constant, v is the frequency, and n is either  $\frac{1}{2}$  or 2 for the direct and indirect band gap transition, respectively. <sup>25,26</sup> The basis for this is derived from eq 3:

$$\alpha h v = A(h v - E_g)^n \tag{3}$$

From the Tauc plot, a linear region at the absorption onset is extrapolated to the x-axis, and the optical band gap is taken as the intercept.<sup>25</sup>

RF Response. The RF response of (PDADMA/MXene)<sub>10</sub> multilayers was also evaluated. A frequency sweep was performed at 1.3 W, and the heating rate was measured as a function of frequency. Samples for RF response testing were prepared on PET. The maximum heating rate corresponded with the resonant frequency for the material and applicator. After determining the resonant frequency, multilayers were exposed to RF fields at the resonant frequency and 10 W. The temperature change with time was then recorded for the samples. Forward looking infrared (FLIR) images were taken of multilayers after exposure to RF fields (32 mW for 5 s) to verify heating of the films.

# ■ RESULTS AND DISCUSSION

**MXene Characterization.** For LbL assembly of nanomaterials, colloidal stability and  $\zeta$ -potential are essential features

toward the success of the deposition. Colloidal stability is desired so that LbL adsorption proceeds uniformly from stepto-step, and a high absolute  $\zeta$ -potential is required so that electrostatic adsorption is favorable. Figure 1a-c shows the Tyndall effect for each of the MXene dispersions, which suggests good colloidal stability. This was further verified by measuring the  $\zeta$ -potential (Figure S1a-c), for which the values were -29.8, -46.0, and -48.7 mV for  $Ti_3C_2T_2$ ,  $Ti_2CT_2$ , and Nb<sub>2</sub>CT<sub>z</sub> dispersions of ~0.05 mg/mL MXene concentration, respectively. The highly negative  $\zeta$ -potential in each case indicates colloidal stability of the nanosheets and verifies that they are each suitable negatively charged components for use in LbL assembly. The nanosheets' hydrodynamic diameters, measured by DLS, were 750, 260, and 215 nm for Ti<sub>3</sub>C<sub>2</sub>T<sub>2</sub>, Ti<sub>2</sub>CT<sub>z</sub>, and Nb<sub>2</sub>CT<sub>z</sub>, respectively (Figure S1d-f); these values are smaller than those observed in the SEM images in Figure 1, described below, likely because of the challenges of DLS in characterizing highly anisotropic materials.

To further confirm the successful MXene synthesis, each dispersion was vacuum filtered to produce a paper for examination using XRD, Figure 1d. In each case, the MXene paper displayed a downshift in  $2\theta$  relative to the parent MAX phase, indicating successful etching and removal of Al from the MAX phase since XRD peaks corresponding to (002) decreased from 9.5 to 7.4°, 13.0 to 7.5°, and 12.8 to 8.0° for  $\text{Ti}_3\text{C}_2\text{T}_{v}$   $\text{Ti}_2\text{CT}_{v}$  and  $\text{Nb}_2\text{CT}_{v}$  respectively, after etching. From Bragg's law, this corresponds to an increase in d-spacing from 0.9 to 1.2 nm, 0.7 to 1.2 nm, and 0.7 to 1.1 nm for  $\text{Ti}_3\text{C}_2\text{T}_{v}$   $\text{Ti}_2\text{CT}_{v}$  and  $\text{Nb}_2\text{CT}_{v}$ , respectively. To verify the MXene morphology, top-down SEM images were obtained for freeze-dried  $\text{Ti}_{n+1}\text{C}_n\text{T}_z$  MXenes and vacuum-filtered  $\text{Nb}_2\text{CT}_z$  MXenes. In the case of freeze-dried  $\text{Ti}_{n+1}\text{C}_n\text{T}_z$  MXenes (Figure

Table 1. Summary of Layer Growth Profiles and Properties of (PDADMA/MXene)<sub>10</sub> Multilayers

$(PDADMA/Ti_3C_2T_z)_{10}$	$(PDADMA/Ti_2CT_z)_{10}$	$(PDADMA/Nb_2CT_z)_{10}$
86 ± 14	$84 \pm 23$	97 <sup>a</sup>
4.9	2.0	7.6
$3.9 \pm 1.2$	$7.3 \pm 1.4$	$6.4 \pm 1.3$
$0.028 \pm 0.001$ at 770 nm	$0.017 \pm 0.004$ at 550 nm	$0.014 \pm 0.002$ at 770 nm
$19.2 \pm 2.8$	$36.0 \pm 11.8$	$28.6 \pm 2.9$
2.8	6.8	10.8
1.87	1.85	1.53
$7.5 \pm 0.8$	$325 \pm 16$	>100,000
$3790 \pm 370$	$9.98 \pm .30$	<0.15
57.9	68.7	78.4
	$86 \pm 14$ 4.9 $3.9 \pm 1.2$ $0.028 \pm 0.001$ at 770 nm $19.2 \pm 2.8$ $2.8$ $1.87$ $7.5 \pm 0.8$ $3790 \pm 370$	$86 \pm 14$ $84 \pm 23$ $4.9$ $2.0$ $3.9 \pm 1.2$ $7.3 \pm 1.4$ $0.028 \pm 0.001$ at 770 nm $0.017 \pm 0.004$ at 550 nm $19.2 \pm 2.8$ $36.0 \pm 11.8$ $2.8$ $6.8$ $1.87$ $1.85$ $7.5 \pm 0.8$ $325 \pm 16$ $3790 \pm 370$ $9.98 \pm .30$

<sup>&</sup>lt;sup>a</sup>(PDADMA/Nb<sub>2</sub>CTz)<sub>10</sub> MXene content was calculated from component and overall film densities.

1e,f), monolayer nanosheets are clearly visible. This indicates the successful exfoliation and delamination of the MXene into nanosheets. For drop-cast Nb<sub>2</sub>CT<sub>z</sub> (Figure 1g), monolayer nanosheets are also visible. However, some few- and multilayer nanosheets are present.

Finally, XPS was used to verify the successful synthesis of MXenes (Figures S2-S5 and Tables S1-S3). XPS survey scans (Figure S2) verify the presence of all four expected elements in each MXene: metal (Ti or Nb), C, O, and F. Each element was deconvoluted into its respective components. For all three MXenes, the presence of C-M-T<sub>z</sub> was confirmed, indicating the successful etching of Al from the MAX phase precursor. The surface functional group ratio was estimated by the ratio of C-M-O<sub>x</sub>:C-M-(OH)<sub>x</sub>:C-M-F<sub>x</sub> component at%. This resulted in an approximate surface functional group ratio, -O:-OH:-F, of 1.2:1.0:1.2 for  $Ti_3C_2T_z$ . In the case of Ti<sub>2</sub>CT<sub>2</sub>, the surface functional group ratio, -O:-OH:-F, was estimated to be 0.9:1.0:0.7. For Nb<sub>2</sub>CT<sub>2</sub>, the -O:-OH:-F ratio was estimated to be 1.6:0.7:0.2. It is important to note that this ratio can be skewed due to oxidation of the MXene during etching, exfoliation, and delamination, particularly in the case of Nb<sub>2</sub>CT<sub>2</sub> which has the highest oxide content of the three MXenes as shown by XPS.

Ti<sub>3</sub>C<sub>2</sub>T<sub>z</sub>, Ti<sub>2</sub>CT<sub>z</sub>, and Nb<sub>2</sub>CT<sub>z</sub> Multilayer Growth. Thin films were fabricated up to 10 LPs by LbL assembly as shown in Figure 2a. PDADMA was selected as the complementary polycation for LbL assembly to electrostatically pair with the negatively charged MXene sheets. Digital images of each film composition at varying LP numbers are depicted in Figure 2bd, in which the films became darker as the number of LPs increased. Tape tests were performed using all three MXene multilayers to ensure sufficient surface adhesion of the film to the substrate (Figure S6). In each case, no visible film was delaminated when removing tape from the films' surfaces. In contrast, drop-cast MXenes easily delaminated and adhered to the tape as shown by An et al.<sup>2</sup> To quantify and confirm the uniform linear growth, thickness, and roughness of (PDAD-MA/MXene), multilayers were examined as a function of the LP number. Profilometric thickness growth profiles (Figure 2e) indicate that films assembled with Ti<sub>3</sub>C<sub>2</sub>T<sub>2</sub>, Ti<sub>2</sub>CT<sub>2</sub>, and  $Nb_2CT_z$  grew as 3.9  $\pm$  1.2, 7.3  $\pm$  1.4, and 6.4  $\pm$  1.3 nm per LP, respectively, as shown in Table 1. In all cases the incremental thickness increased linearly, consistent with uniform layer growth. Profilometric film roughness values were also measured and determined to be 19.2, 36, and 28.6 nm for  $(PDADMA/Ti_3C_2T_z)_{10}$ ,  $(PDADMA/Ti_2CT_z)_{10}$ , and  $(PDAD-Ti_2CT_z)_{10}$ .  $MA/Nb_2CT_z)_{10}$  multilayers, respectively (Figure 2f). In contrast, local roughness verified by AFM (Figures S7-S9)

was considerably lower; specifically, the local roughness values were 2.8, 6.8, and 10.8 nm for  $(PDADMA/Ti_3C_2T_2)_{10}$ ,  $(PDADMA/Ti_2CT_z)_{10}$ , and  $(PDADMA/Nb_2CT_z)_{10}$  multilayers, respectively. The variations in profilometric vs AFM roughnesses are ascribed to the differences in measurement length scales. Profilometric roughness is measured over a line scan with a length of 0.4 mm, whereas the AFM roughness uses a 10  $\mu$ m by 10  $\mu$ m area. The sheet morphologies can be seen on the surface of the  $(PDADMA/Ti_3C_2T_z)_{10}$  multilayers (Figure S7b-d), in which the MXene sheets appear to lay flat, possibly contributing to the lower local roughness. The overall higher roughnesses for (PDADMA/Ti<sub>2</sub>CT<sub>z</sub>)<sub>10</sub> and (PDAD- $MA/Nb_2CT_z$ )<sub>10</sub> multilayers are attributed to the formation of oxides on the surface of the films as seen in the AFM phase images. As shown later, these two multilayer types are highly prone to oxidation relative to the  $(PDADMA/Ti_3C_2T_z)_{10}$ multilayers.

Gravimetric growth of the films was next explored using QCM (Figure 2g) to determine the incremental mass deposited per LP, the multilayer densities, and the PDADMA:MXene composition within the multilayer (Table 1).  $(PDADMA/Nb_2CT_z)_v$  multilayers had the largest incremental areal mass followed by (PDADMA/Ti<sub>3</sub>C<sub>2</sub>T<sub>z</sub>)<sub>v</sub> and then (PDADMA/Ti<sub>2</sub>CT<sub>z</sub>)<sub>v</sub>. Accordingly, the density was calculated with knowledge of the areal masses and thicknesses (Table 1). The densities of the multilayers followed the same trend as incremental areal mass and directly correlated with the molecular weights of the respective MXene. The densities of PDADMA/ $Ti_3C_2T_z$  and PDADMA/ $Nb_2CT_z$  multilayers were similar to the densities of the pure MXene powder (4.21 g/cm<sup>3</sup> for  $Ti_3C_2T_x$  and 7.8 g/cm<sup>3</sup> for  $Nb_2CT_x$ , respectively).<sup>27,28</sup> However, the density of the PDADMA/Ti<sub>2</sub>CT<sub>2</sub> multilayer was considerably lower than that of pure  $Ti_2CT_z$  (4.4 g/cm<sup>3</sup>), which may indicate a looser multilayer structure.<sup>29</sup> From previous LbL work, an increase in film porosity is observed for LbL-assembled films as compared to vacuum-filtered films.<sup>30</sup> Based on the cross-sectional morphology of (PDADMA/  $Ti_3C_2T_z$ ) multilayers assembled in our prior work, we expect a similar increase in porosity in our multilayers, which would result in the lower bulk film density. Additionally, it is possible that the in situ oxidation of Ti<sub>2</sub>CT<sub>z</sub> during the LbL assembly process further lowers the bulk film density. As Ti<sub>2</sub>CT<sub>z</sub> oxidizes, the material is lost as gaseous oxidation byproducts, which would result in a decrease in overall film mass and a possible increase in porosity due to the formation of gases.<sup>31</sup> The formation of small TiO<sub>2</sub> particles could also increase the interlayer spacing between nanosheets and lead to the formation of larger macropores.32

MXene content in each of the films was calculated to be 86  $\pm$  14 and 84  $\pm$  23 for (PDADMA/Ti<sub>3</sub>C<sub>2</sub>T<sub>z</sub>)<sub>10</sub> and (PDADMA/Ti<sub>2</sub>CT<sub>z</sub>)<sub>10</sub> multilayers, respectively. (The high error is attributed to batch-to-batch variation in the MXenes produced.) In the case of (PDADMA/Nb<sub>2</sub>CT<sub>2</sub>)<sub>10</sub> multilayers, a decrease in areal mass was observed after the polymer deposition step, making it infeasible to determine MXene content. The decrease in mass can be attributed to the removal of loosely adhered Nb<sub>2</sub>CT<sub>z</sub> and a change in hydration.<sup>33</sup> Using a density of 7.8 g/cm<sup>3</sup> for commercial Nb<sub>2</sub>C (American Elements) and a PDADMA density of 1.2 g/cm<sup>3</sup>, the Nb<sub>2</sub>C content of  $(PDADMA/Nb_2CT_z)_{10}$  was determined to be 97%. The number of MXene nanosheets per layer pair was then estimated from the incremental thickness. For this calculation, we assumed that the monolayer nanosheet thicknesses were 1. 1, and 0.3 nm for Ti<sub>3</sub>C<sub>2</sub>T<sub>z</sub>, Ti<sub>2</sub>CT<sub>z</sub>, and Nb<sub>2</sub>CT<sub>z</sub> MXenes, respectively. 4,34,35 This leads to an estimate that roughly 4, 7, and 21 nanosheets are deposited per LP for Ti<sub>3</sub>C<sub>2</sub>T<sub>2</sub>, Ti<sub>2</sub>CT<sub>2</sub>, and Nb<sub>2</sub>CT<sub>z</sub>, respectively. The higher number of nanosheets deposited per LP of Nb<sub>2</sub>CT<sub>z</sub> is likely due to the presence of multiple layers of MXenes as flakes in the dispersion, which were observable using SEM and DLS.

Meanwhile, all of the growth rates are the same order of magnitude; the MXenes with n=1 demonstrate slightly higher growth rates. This could be attributed to differences in the  $\zeta$ -potentials, in which  ${\rm Ti_2CT_z}$  and  ${\rm Nb_2CT_z}$  exhibited values (-46.0 and -48.7 mV, respectively) far higher than that of  ${\rm Ti_3C_2T_x}$  (-29.8 mV). We speculate that MXenes that are more negatively charged adsorb and adhere to the surface more readily and are more difficult to wash away during assembly, leading to a higher growth rate.

Top-down SEM images of the multilayers on PET substrates are shown in Figure 3. The surface morphology of the films

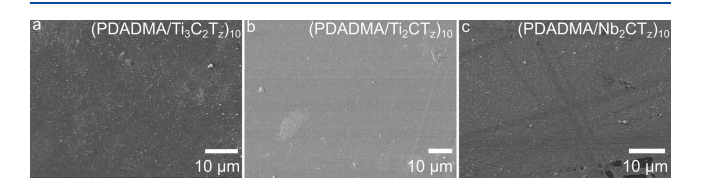


**Figure 3.** Top-down SEM images of (a)  $(PDADMA/Ti_3C_2T_z)_{10}$ , (b)  $(PDADMA/Ti_2CT_z)_{10}$ , and (c)  $(PDADMA/Nb_2CT_z)_{10}$  multilayers. In all cases, the MXene was the topmost layer.

was largely uniform, supporting the low roughness of the films. However, there were some scratches observed for (PDADMA/Nb<sub>2</sub>CT<sub>z</sub>)<sub>10</sub> multilayers (Figure 3c), which may be a result of sample handling. Also, small particulates adsorbed on the surface may be attributed to dust particles or oxidation products. Regarding the cross-sectional morphology of these multilayers, our previous work with PDADMA/Ti<sub>3</sub>C<sub>2</sub> multilayers has shown that LbL assembly results in a layered structure with well-aligned and alternating layers of MXene and the polymer.<sup>2</sup> Given the similar assembly method and nature of the constituent materials, we expect a similar structure for the multilayers fabricated in this work.

UV—vis absorbance was also measured as a function of the LP number, Figure 4a—c. In each case, absorbance increased with increasing LP number, indicating a darker film and more MXene nanosheets being deposited. Peak wavelengths were observed at 770, 550, and 770 nm for (PDADMA/ ${\rm Ti}_3{\rm C}_2{\rm T}_z$ )<sub>10</sub>, (PDADMA/ ${\rm Ti}_2{\rm CT}_z$ )<sub>10</sub>, and (PDADMA/ ${\rm Nb}_2{\rm CT}_z$ )<sub>10</sub> multilayers, respectively. Absorbance at the peak wavelength as a

function of the LP number for each film composition is shown in Figure 4d. The absorbance growth profiles confirm linear growth of the films.

**Electro-Optical Properties.** Electrical properties, specifically sheet resistance  $(R_s)$  and DC conductivity  $(\sigma_{DC})$ , were also measured as a function of the LP number (Figure 4e) to determine when percolation of the MXene throughout the film was achieved. Due to the low conductivity of Nb<sub>2</sub>CT<sub>2</sub>, the electrical properties of Nb<sub>2</sub>CT<sub>z</sub>-based films could not be quantified within the instrument's range and were, thus, not reported here. 17 The low conductivity can also be attributed to the high ratio of -O terminal groups to -F terminal groups in Nb<sub>2</sub>CT<sub>2</sub> as seen in XPS. Previous studies have shown that -Oterminated MXenes have the lowest density of states at the Fermi level, whereas -F-terminated MXenes have the highest density of states, which would support the low conductivities observed here. 19 Moreover, Nb<sub>2</sub>CT<sub>z</sub> MXenes are extremely prone to oxidation, as demonstrated by the oxide peak at  $\sim$ 207 and ~530 eV in the Nb 3d and O 1s XPS component spectra, respectively (Figure S5a-c).21 In conjunction with the presence of an insulating polymer, these factors result in a lower conductivity of the (PDADMA/Nb<sub>2</sub>CT<sub>z</sub>)<sub>v</sub> multilayers as compared to Nb<sub>2</sub>CT<sub>2</sub> MXene films prepared by VAF (500 S/ m). <sup>14</sup> Additionally, Nb<sub>2</sub>CT<sub>z</sub> films prepared by in situ etching of the sputtered MAX phase demonstrated a resistivity 2 orders of magnitude higher than that of its Ti<sub>2</sub>CT<sub>z</sub> MXene counterpart prepared in the same method. 17 This would correspond with a  $\sigma_{\rm DC}$  of 0.1 S/m for (PDADMA/Nb<sub>2</sub>CT<sub>z</sub>)<sub>10</sub> multilayers based on the measured  $\sigma_{\rm DC}$  of (PDADMA/Ti<sub>2</sub>CT<sub>z</sub>)<sub>10</sub> multilayers, which is below the limitations of our four-point probe (0.15 S/ m). However, electrical percolation of the MXene was reached by three LPs and five LPs for  ${\rm Ti_3C_2T_z}$ - and  ${\rm Ti_2CT_z}$ -based films, respectively, with the former displaying a  $\sigma_{DC}$  3 orders of magnitude higher than that of the latter. This is in agreement with theoretical studies of the electronic band gap of  $Ti_{n+1}C_nT_z$ MXenes and experimentally reported MXene conductivities. 14,19 This result is attributed to the additional internal layer of Ti that does not interact with the surface functional groups in Ti<sub>3</sub>C<sub>2</sub>T<sub>z</sub> as compared to Ti<sub>2</sub>CT<sub>z</sub>. This results in more Ti that can contribute to the density of states (DOS) at the Fermi level and the observed conductivity increase. However, both (PDADMA/ $T_{n+1}C_nT_z$ ), multilayers exhibit considerably lower  $\sigma_{DC}$  than their MXene-only film counterparts due to the inclusion of the insulating PDADMA and oxidation during film assembly. The latter issue is more pronounced for (PDADMA/Ti<sub>2</sub>CT<sub>z</sub>), multilayers due to the worsened oxidative stability of Ti<sub>2</sub>CT<sub>z</sub> as compared to Ti<sub>3</sub>C<sub>2</sub>T<sub>z</sub>.<sup>20</sup> For comparison,  ${\rm Ti_3C_2T_z}$  films reach  $\sigma_{\rm DC}$  values of 240,000 to 857,000 S/m for vacuum-filtered films and 309,200 to 650,000 S/m for spin-cast films.  $^{12,14,36,37}$  Ti $_2$ CT $_z$  films report a  $\sigma_{\rm DC}$  of 161,000 S/m for vacuum-filtered films, 525,000 S/m for spincast films, and 550,000 S/m for nonsurface-terminated Ti<sub>2</sub>C from theoretical calculations. 14,38,39

Interestingly, the conductivity of  ${\rm Ti_2CT_z}$ -based films decreased with the increasing LP number. We attribute this observation to the poor oxidative stability of  ${\rm Ti_2CT_z}$ . Specifically, LbL assembly is a water-based process requiring approximately an hour per LP, and water exposure is known to accelerate the oxidation of  ${\rm Ti_2CT_z}^{20}$  In comparison, oxidation for  ${\rm Ti_3C_2T_z}$  is much slower and thus less affected during the LbL assembly process. In support, visible oxidation products (particulate matter on the surface, Figure S8) were present in AFM surface images of the (PDADMA/ ${\rm Ti_2CT_z}$ ) multilayers.

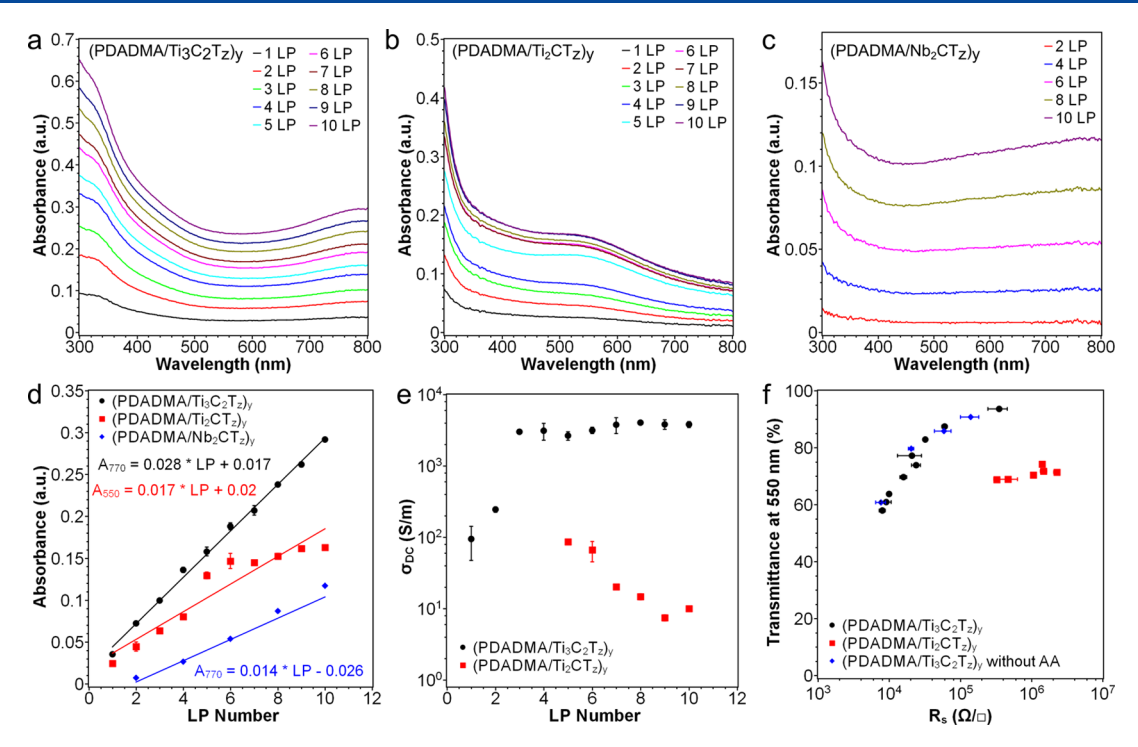


Figure 4. UV—vis absorbance as a function of wavelength for varying LP numbers of (a) (PDADMA/ $Ti_2C_2T_z$ ), (b) (PDADMA/ $Ti_2CT_z$ ), and (c) (PDADMA/ $Nb_2CT_z$ ), multilayers. (d) Absorbances at 770, 550, and 770 nm as a function of the LP number for the three respective multilayers. (e) DC conductivity with LP number for (PDADMA/ $Ti_3C_2T_z$ ), and (PDADMA/ $Ti_2CT_z$ ), multilayers. (f) Transmittance at 550 nm vs sheet resistance for (PDADMA/ $Ti_{n+1}C_nT_z$ ), multilayers with ascorbic acid (AA) in the assembly baths and (PDADMA/ $Ti_3C_2T_z$ ), without AA. DC conductivity and sheet resistance for (PDADMA/ $Nb_2CT_z$ ), multilayers and (PDADMA/ $Ti_2CT_z$ ), for four or less LPs could not be determined because the samples were too resistive.

Table 2. Optical Properties of (PDADMA/MXene)<sub>10</sub> Multilayers

			Optical band gap (eV)	
MXene multilayer	Absorption coefficient at 550 nm (cm <sup>-1</sup> ) <sup>a</sup>	Optical conductivity at 550 nm $(S/cm)^b$	Direct <sup>c</sup>	Indirect <sup>d</sup>
$(PDADMA/Ti_3C_2T_z)_{10}$	$1.45 \times 10^{5}$	444	3.05	1.61
$(PDADMA/Ti_2CT_z)_{10}$	$4.69 \times 10^4$	137	3.80	3.01
$(PDADMA/Nb_2CT_z)_{10}$	$3.73 \times 10^4$	105	3.67	2.47

<sup>a</sup>The absorption coefficient was calculated using eq 1. <sup>b</sup>Optical conductivity was calculated using eq 2. <sup>c</sup>Direct optical band gap was obtained from Figure S11d-f. <sup>d</sup>Indirect optical band gap was obtained from Figure S11a-c.

These films were all made using ascorbic acid, which slows oxidation; in a very recent work, we showed that citric acid (CA) is also an antioxidant for MXenes.  $^{20,22}$  We fabricated (PDADMA/ $\mathrm{Ti_2CT_2}$ ) $_y$  films using CA in place of AA as the antioxidant, and we found largely the same trend in conductivity with LP numbers (Figure S10). These results indicate that future optimization of the LP number and deposition time is needed as well as increased measures to mitigate oxidation to preserve the conductivity. Possible methods for this include reducing deposition time, increasing MXene concentration, reducing bath temperature (e.g., ice bath), adding Ar bubbling, and exploring other antioxidants.  $^{22,40,41}$ 

The performance of Ti-based MXene multilayers as transparent conductive films (TCFs) was assessed due to their conductance and transparency. A plot comparing sheet resistance and transmittance at 550 nm of (PDADMA/ $Ti_{n+1}C_nT_z$ )<sub>y</sub> multilayers is shown in Figure 4f. Ideal TCFs demonstrate low sheet resistances and high transmittances. We also compared the properties of  $Ti_3C_2$ -based films assembled both with and without an antioxidant and found the properties to be unaffected. Meanwhile, (PDADMA/ $Ti_3C_2T_z$ )<sub>10</sub> multi-

layers significantly outperforms (PDADMA/ ${\rm Ti_2CT_z}$ )<sub>10</sub> multilayers in terms of both sheet resistance and transmittance; both are poorer than the performance of pure  ${\rm Ti_3C_2T_z}$  films.  $^{12,14}$ This is due to the inclusion of the insulating PDADMA, which is required for the LbL assembly process. However, we note that the benefit of the LbL assembly process is that it produces adherent films on a variety of surfaces, which is otherwise challenging for MXenes alone.  $^2$ 

From previous reports, we also expect the optical properties of the films to vary depending on the MXene used for assembly. To explore how this effect translated to LbL assemblies, we compared the refractive index, absorption coefficient, optical conductivity, and direct and indirect optical band gaps of the three types of MXene multilayers. Refractive indices for the multilayers are summarized in Table 1. (PDADMA/ $Ti_3C_2T_z$ )<sub>10</sub> multilayers had the highest refractive index followed closely by (PDADMA/ $Ti_2CT_z$ )<sub>10</sub>, with (PDADMA/ $Nb_2CT_z$ )<sub>10</sub> having the lowest refractive index.

Table 2 summarizes the absorption coefficient, optical conductivity, and direct and indirect optical band gaps for each  $(PDADMA/MXene)_{10}$  investigated. The absorption coefficient,  $\alpha$ , allows for a comparison of how transparent

thin films will be at a given thickness. As such, having a low absorption coefficient is beneficial for transparent conductive films as it allows for higher transparencies at the same thicknesses. From Table 2, Ti<sub>2</sub>C-based multilayers possess an absorption coefficient at 550 nm that is an order of magnitude lower than that of Ti<sub>3</sub>C<sub>2</sub>-based multilayers. Nb<sub>2</sub>C-based films demonstrated the lowest absorption coefficient, indicating that these films are the most transparent at this wavelength for the same thickness. Compared to previous reports of spin-cast  ${\rm Ti_3C_2T_z}$  and  ${\rm Ti_2CT_z}$  films with an  $\alpha_{550}$  of  $2.3\times10^5$  and  $2.7\times10^5$ 10<sup>5</sup> cm<sup>-1</sup>, respectively, and sputtered Ti<sub>2</sub>CT<sub>z</sub> and Nb<sub>2</sub>CT<sub>z</sub> films with an  $\alpha_{550}$  of 2.2  $\times$  10<sup>5</sup> and 5.7  $\times$  10<sup>5</sup> cm<sup>-1</sup>, respectively, the LbL-assembled multilayers herein have lower  $\alpha_{550}$  values, indicating that less light will be absorbed for the same thickness. 17,36,38 Optical conductivities were calculated from the thicknesses and transmittances of the thin films following eq 2. As expected, the optical conductivity of Ti<sub>3</sub>C<sub>2</sub>based films was the highest at 444 S/cm. Nb<sub>2</sub>C-based films possessed the lowest optical conductivity, which corresponds with Nb<sub>2</sub>C-based films demonstrating the worst electrical properties.

The next property of interest was the optical band gap of the films, which can be used to evaluate the applicability of the films for photonic devices (e.g., solar cells and LEDs).44 Optical band gap can be divided into two categories: direct and indirect. <sup>45</sup> The direct band gap energy is the energy a photon needs to be excited from the valence band to the conduction band without the assistance of a phonon. In contrast, the indirect band gap energy is the energy required to excite a photon with the assistance of a phonon. Due to this distinction, direct band gap materials tend to be favorable because they only require photons, making excitation more likely to occur and subsequently faster. Direct and indirect optical band gaps were obtained for each film composition using Tauc plots (Figure S11 and Table 2). (PDADMA/  $Ti_3C_2T_z$ )<sub>10</sub> multilayers possessed the lowest direct and indirect band gaps followed by (PDADMA/Nb<sub>2</sub>CT<sub>z</sub>)<sub>10</sub> then (PDAD- $MA/Ti_2CT_2$ )<sub>10</sub> multilayers. This trend is in agreement with the observations of Velusamy et al. for the photoresponse of pure MXene thin films. 43

Previous reports for pure  ${\rm Ti_3C_2T_z}$  films demonstrated a direct band gap of 1.05 eV when prepared using VAF and  $\sim 3.9$  eV when prepared by electrohydrodynamic atomization (EHDA). For Nb<sub>2</sub>CT<sub>z</sub> powders, a direct band gap of 1.47 eV was reported. However, band gaps are highly dependent on the surface functional group distribution and synthesis method of MXene, making it difficult to compare. Additionally, PDADMA has a direct band gap of 4 eV, which likely contributes to the higher band gap of the (PDADMA/MXene)<sub>10</sub> multilayers as compared to the pure MXene films prepared using VAF.

**Oxidative Stability of the Multilayers.** MXenes are notably prone to oxidation, which leads to changes in both color and electrical properties.  $^{20,21,40,41,49-51}$  It is likely that MXene-based TCFs that do not take measures against oxidation will exhibit a worsened performance over time. For example, Lee *et al.* demonstrated that as-prepared  $\mathrm{Ti_3C_2T_z}$  films fabricated using spin-casting oxidized significantly in a matter of hours when stored at 70 °C and 100% RH.  $^{52}$  On the other hand, films treated by thermal or  $\mathrm{H_2}$  annealing demonstrated minimal increases in electrical resistance, indicating improved oxidative stability.  $^{52,53}$  Recently, our group has also demonstrated that the inclusion of  $\mathrm{Ti_3C_2T_z}$  in

polymer matrices, specifically polyvinyl alcohol, can slow the rate of oxidation. <sup>40</sup> Influenced by this, we sought to understand the nature of MXene oxidation in LbL assemblies.

Due to MXene-based composites being prone to oxidation, both UV–vis absorbance and  $\sigma_{\rm DC}$  were monitored over the course of several months as proxies for the degree of oxidation of the MXene-based multilayers. When MXene nanosheets oxidize, they degrade into their respective metal oxides. This results in a change in color that is quantifiable by UV–vis spectrophotometry. As such, monitoring how the absorbance of the multilayer changes over time is a viable option for qualifying the oxidation process. The absorbances of (PDADMA/Ti<sub>2</sub>C<sub>2</sub>T<sub>z</sub>)<sub>10</sub>, (PDADMA/Ti<sub>2</sub>CT<sub>z</sub>)<sub>10</sub>, and (PDADMA/Nb<sub>2</sub>CT<sub>z</sub>)<sub>10</sub> multilayers as a function of time are shown in Figure 5. The gap in the data is due to lab closures during the

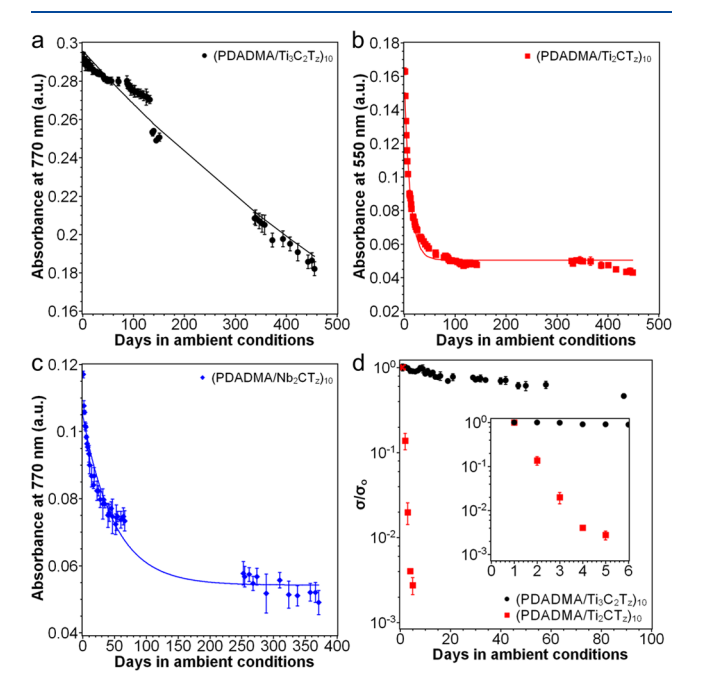


**Figure 5.** Absorbance changes over time for (a) (PDADMA/  $Ti_3C_2T_z)_{10}$ , (b) (PDADMA/ $Ti_2CT_z)_{10}$ , and (c) (PDADMA/  $Nb_2CT_z)_{10}$  multilayers. The lines represent absorbances from the model fitting (eq 3). (d) Normalized conductivities of (PDADMA/  $Ti_3C_2T_z)_{10}$  and (PDADMA/ $Ti_2CT_z)_{10}$  multilayers over time. Inset shows the first 6 days of measurements. DC conductivity for (PDADMA/ $Nb_2CT_z)_y$  multilayers could not be determined because the samples were too resistive.

COVID-19 lockdown. Absorbance was monitored at the peak wavelengths for each case: 770, 550, and 770 nm for (PDADMA/Ti<sub>3</sub>C<sub>2</sub>T<sub>z</sub>)<sub>10</sub>, (PDADMA/Ti<sub>2</sub>CT<sub>z</sub>)<sub>10</sub>, and (PDADMA/Nb<sub>2</sub>CT<sub>z</sub>)<sub>10</sub> multilayers, respectively. The absorbance of the (PDADMA/Ti<sub>3</sub>C<sub>2</sub>T<sub>z</sub>)<sub>10</sub> multilayer decreased linearly over time at a rate of 0.00024 a.u. or 0.08% per day. This corresponds to an 88% retention in absorbance at 770 nm for over 4 months and 64% after 450 days, indicating an improved oxidative stability as compared to other MXenes in the literature, which did not use an antioxidant or LbL process.  $^{41,52,53}$  On the other hand, the absorbance of the (PDADMA/Ti<sub>2</sub>CT<sub>z</sub>)<sub>10</sub> multilayer decreased rapidly early on and eventually equilibrated, indicating a higher reaction order for oxidation and worsened oxidative stability relative to the Ti<sub>3</sub>C<sub>2</sub>T<sub>z</sub>-based multilayer, which is in agreement with previous findings for our groups for Ti<sub>n+1</sub>C<sub>n</sub>T<sub>z</sub> dispersions. The

Table 3. Fitting Parameters from the Change in Multilayer Absorbance Due to Oxidation with Time

Film	$\tau$ (days)	$A_{ m unre}$	$A_{ m re}$	$A_{\rm re}/(A_{\rm re} + A_{\rm unre})$	$t_{1/2}$ (days)
$(PDADMA/Ti_3C_2T_z)_{10}$	1010	0.00	1.01	1.00	701
$(PDADMA/Ti_2CT_z)_{10}$	11.8	0.31	0.67	0.68	8.18
$(PDADMA/Nb_2CT_z)_{10}$	49.4	0.46	0.44	0.48	34.3

improved oxidative stability of  ${\rm Ti_3C_2T_z}$ -based multilayers is attributed to the presence of protected inner Ti layers. <sup>21</sup> Prior work has demonstrated that surface-terminated MXenes are more oxidatively stable. This is likely due to the increased Bader charge of surface-terminated Ti as compared to bare Ti, which would result in them being more likely to react with the water molecules that induce oxidation. <sup>54,55</sup> Lastly, the absorbance of the (PDADMA/Nb<sub>2</sub>CT<sub>z</sub>)<sub>10</sub> multilayer followed a trend similar to that of the (PDADMA/Ti<sub>2</sub>CT<sub>z</sub>)<sub>10</sub> multilayer. To quantify the rate of absorbance decay, reaction time constants and the portion of the film that reacted (*i.e.*, oxidized) was determined by fitting eq 4 to the experimental data following previous reports: <sup>41,56</sup>

$$A = A_{\rm unre} + A_{\rm re}e^{(-t)/\tau} \tag{4}$$

where A is the absorbance,  $A_{\mathrm{unre}}$  is the unreacted portion,  $A_{\mathrm{re}}$  is the reacted portion, and  $\tau$  is the time constant in days. The resultant fitting parameters are shown in Table 3, and predicted absorbances from the model are shown in Figure 5a-c. From the reaction time constants, multilayers assembled with MXenes with n = 1 had the shortest shelf lives.  $(PDADMA/Ti_2CT_z)_{10}$  and  $(PDADMA/Nb_2CT_z)_{10}$  had time constants of 11.8 and 49.4 days, respectively, indicating that the latter was more oxidatively stable. The (PDADMA/  $Ti_3C_2T_z)_{10}$  multilayer had a time constant  $\tau$  of 1010 days, which was 2 and 1 orders of magnitude higher than those of  $(PDADMA/Ti_2CT_z)_{10}$  and  $(PDADMA/Nb_2CT_z)_{10}$ , respectively, indicating that (PDADMA/Ti<sub>3</sub>C<sub>2</sub>T<sub>z</sub>)<sub>10</sub> was the most stable. Another representation of the rate of oxidation is the absorbance half-life  $(\tau_{1/2})$ , or the amount of time taken for a multilayer to lose half of  $A_{re}$ , which was determined using eq 5:

$$\tau_{1/2} = \ln(2) \times \tau \tag{5}$$

The half-life for the  $(PDADMA/Ti_3C_2T_z)_{10}$  multilayer was 701 days, which was 59 and 14 times longer than those of  $(PDADMA/Ti_2CT_z)_{10}$  and  $(PDADMA/Nb_2CT_z)_{10}$ , respectively. It is important to note that differences in nanosheet thickness, mono- vs few-layer nanosheets, and lateral size can greatly affect the rate of oxidation, making direct comparisons difficult. 41,57 Lastly, the ratio of  $A_{\text{unre}}$  to  $A_{\text{unre}} + A_{\text{re}}$ , which is indicative of the fraction of the film that will oxidize given an infinite amount of time,  $^{56}$  was considered. Lower ratios of  $A_{\rm unre}$ to  $A_{\text{unre}}$  +  $A_{\text{re}}$  for (PDADMA/Ti<sub>2</sub>CT<sub>z</sub>)<sub>10</sub> and (PDADMA/  $Nb_2CT_z$ )<sub>10</sub> correspond with a higher unreacted component. Because the fitting is based on the UV-vis absorbance of the films, the color of the metal oxide can contribute to the  $A_{unre}$ value, making the unreacted component artificially higher. To account for this,  $\tau$  and  $\tau_{1/2}$  were both calculated based on the reactive portion. It is also possible that once a sufficiently thick layer of oxides has formed, the oxide and polymer act as a barrier that protects the MXenes from further oxidation.

Due to the semiconductive nature of the metal oxide formed,  $^{40,58,59}$  the  $\sigma_{\rm DC}$  of the MXene-based multilayers also decreased over time. As such, monitoring how  $\sigma_{\rm DC}$  changes is another method for qualifying the oxidation process. The normalized  $\sigma_{\rm DC}$  values of (PDADMA/Ti<sub>3</sub>C<sub>2</sub>T<sub>z</sub>)<sub>10</sub> and

(PDADMA/Ti<sub>2</sub>CT<sub>2</sub>)<sub>10</sub> as a function of time are shown in Figure 5d. The  $\sigma_{DC}$  for the (PDADMA/Nb<sub>2</sub>CT<sub>z</sub>)<sub>10</sub> was too low to measure within the instrumentation's bounds and was not considered. The significantly lower  $\sigma_{\rm DC}$  of Nb<sub>2</sub>CT<sub>z</sub>-based multilayers as compared to Ti<sub>2</sub>CT<sub>z</sub>-based multilayers is in agreement with previous reports from literature studies. 14,17 As with absorbance, the  $\sigma_{DC}$  of (PDADMA/Ti<sub>3</sub>C<sub>2</sub>T<sub>z</sub>)<sub>10</sub> decreased linearly over time at a rate of 23 S/m per day. This demonstrates that both absorbance and conductivity are viable methods for monitoring the oxidation process for MXenebased films. Further, this result shows that the rate of oxidation of the (PDADMA/Ti<sub>3</sub>C<sub>2</sub>T<sub>z</sub>)<sub>10</sub> multilayer was lower as compared to the (PDADMA/Ti<sub>2</sub>CT<sub>z</sub>)<sub>10</sub> multilayer, which is in agreement with previous studies from our group.  $^{20}$  The  $\sigma_{\rm DC}$ of the (PDADMA/Ti<sub>2</sub>CT<sub>z</sub>)<sub>10</sub> multilayer decreased exponentially and then was too low for reliable measurement after 5 days. The inability to measure  $\sigma_{
m DC}$  of the (PDADMA/  $Ti_2CT_2$ )<sub>10</sub> multilayer coincides with the disappearance of the absorbance peak at 550 nm (Figure S12). As such, Ti<sub>2</sub>CT<sub>z</sub>based multilayers are especially prone to oxidation as compared to Ti<sub>3</sub>C<sub>2</sub>T<sub>z</sub>-based multilayers despite the use of an antioxidant.

RF Heating of (PDADMA/MXene)<sub>10</sub> Multilayers. Given the conductivity of the Ti-based MXene multilayers, we next explored their responses to RF fields. When exposed to alternating RF fields, polarized molecules and charged ions in the film will begin to rotate or collide in order to align with the field, leading to frictional losses as heat.<sup>60</sup> This heating is typically rapid and highly localized, making RF heating useful for a number of applications including welding, heating food, and curing.<sup>61–64</sup> However, materials with low conductivity do not undergo RF heating because there is no electrical percolating network.<sup>65</sup> On the other hand, materials with high conductivity tend to reflect the RF fields, resulting in no heating.<sup>65,66</sup> In this manner, the RF heating response may be considered as a proxy for the electrical properties of the (PDADMA/MXene)<sub>10</sub> multilayers.

First, a frequency sweep at 1.3 W was performed to determine the frequency for peak heating of the materials for the specific applicator used as shown in Figure 6a. A lower power was used for the sweep to ensure that the MXene did not oxidize due to temperature excursions. The peak heating rate occurred at a frequency of 135 MHz. Then, the RF heating response at 10 W and 135 MHz was determined as shown in Figure 6b. As expected, the  $(PDADMA/Ti_3C_2T_z)_{10}$  multilayer demonstrated the largest temperature change as compared to both  $(PDADMA/Ti_2CT_z)_{10}$  and  $(PDADMA/Nb_2CT_z)_{10}$ multilayers when exposed to RF waves. Specifically, the temperature of the (PDADMA/Ti<sub>3</sub>C<sub>2</sub>T<sub>z</sub>)<sub>10</sub> multilayer increased from ~23 to ~103 °C in ~35 s upon application of the field. A forward looking infrared (FLIR) image of a  $(PDADMA/Ti_3C_2T_z)_{10}$  multilayer is shown in Figure S13 and confirms localized heating of the multilayer as opposed to the surroundings. Thermal images of the other multilayers were not included because they did not exhibit RF-induced heating. Even so, the heating rate for the  $(PDADMA/Ti_3C_2T_z)_{10}$ 

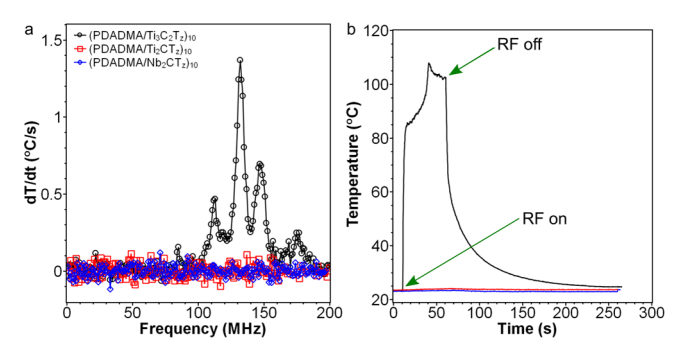


**Figure 6.** (a) Heating rate at varying frequencies for (PDADMA/MXene)<sub>10</sub> multilayers at 1.3 W. (b) Temperature response with RF exposure (10 W at 135 MHz) for (PDADMA/MXene)<sub>10</sub> multilayers. RF exposure turned on at 10 s and off at 60 s.

multilayers is lower than that of our prior work with poly(vinyl alcohol)/MXene composites ( $\sim 3~\mu m$  thick). This difference may be attributed to the different applied powers or, as more likely, our considerably thinner films, which may more rapidly dissipate heat into the environment. Regardless, the (PDADMA/Ti<sub>3</sub>C<sub>2</sub>T<sub>z</sub>)<sub>10</sub> multilayers displayed rapid and localized heating when exposed to alternating RF fields, indicating promise for use in RF heating applications.

#### CONCLUSIONS

In this work, we successfully fabricated thin films via LbL assembly with chemically and structurally diverse MXenes and demonstrated how MXene type influences the electronic and optical properties of the film. This also allowed for a comparison of the oxidative stability and RF heating response. As expected, Ti-based MXenes demonstrate more metal-like behavior as compared to Nb-based MXenes, as shown by the optical and electrical conductivities. Additionally, we experimentally confirmed the effect of n on both oxidative stability and electrical properties by demonstrating longer shelf life and higher conductivity of  $\text{Ti}_3\text{C}_2\text{T}_z$ -based thin films as compared to  $\text{Ti}_2\text{CT}_z$ -based thin films. More importantly, we were able to demonstrate that  $(\text{PDADMA/Ti}_3\text{C}_2\text{T}_z)_{10}$  multilayers possessed half-lives on the order of years when stored under ambient conditions, indicating considerable promise for these films.

Establishing the ability to fabricate thin films using LbL assembly with nonconventional MXenes provides a highly controlled and tunable film assembly process to explore a variety of applications for the future. However, the persistent issue of oxidation remains a challenge. The slower oxidation and higher  $\sigma_{DC}$  of MXenes with higher n indicate promise for more layered MXenes. While the properties measured herein indicate an improved performance of (PDAMA/Ti<sub>3</sub>C<sub>2</sub>T<sub>z</sub>)<sub>v</sub> multilayers as compared to (PDADMA/M<sub>2</sub>CT<sub>z</sub>)<sub>v</sub> multilayers, this study did not fully explore all possible properties and applications of the multilayers. Prior work has shown that Ti<sub>2</sub>CT<sub>2</sub> and Nb<sub>2</sub>CT<sub>2</sub> MXene-based composites can demonstrate improved metrics as compared to Ti<sub>3</sub>C<sub>2</sub>T<sub>z</sub> MXene-based composites for photocatalytic H2 evolution for both MXenes, methane adsorption for Ti<sub>2</sub>CT<sub>z</sub>, lubricants for Nb<sub>2</sub>CT<sub>z</sub>, and biocompatibility for Nb<sub>2</sub>CT<sub>z</sub>. Additionally, Ti<sub>2</sub>CO<sub>2</sub> has been predicted to be semiconducting, in contrast to the metallic nature of Ti<sub>3</sub>C<sub>2</sub>T<sub>z</sub>. <sup>19</sup> Therefore, these applications may prove to be promising avenues to explore in the future for these LbL assemblies.67-7

#### ASSOCIATED CONTENT

# Supporting Information

The Supporting Information is available free of charge at https://pubs.acs.org/doi/10.1021/acs.langmuir.1c01904.

Experimental procedure for XPS deconvolution;  $\zeta$ -potential, DLS size distribution, XPS survey scans, and peak fitting results for  ${\rm Ti_3C_2T_2}$ ,  ${\rm Ti_2CT_2}$ , and  ${\rm Nb_2CT_2}$  MXenes; tape adhesion testing, AFM surface scans, and AFM phase images of (PDADMA/MXene)<sub>10</sub> multilayers;  $\sigma_{\rm DC}$  of (PDADMA/Ti<sub>2</sub>CT<sub>z</sub>)<sub>y</sub> multilayers assembled in the presence of citric acid; Tauc plots and full UV–vis absorbance spectra with increasing storage time of (PDADMA/MXene)<sub>10</sub> multilayers; and the FLIR image of (PDADMA/Ti<sub>3</sub>C<sub>2</sub>T<sub>z</sub>)<sub>10</sub> multilayer after RF exposure (PDF)

#### AUTHOR INFORMATION

#### **Corresponding Author**

Jodie L. Lutkenhaus — Artie McFerrin Department of Chemical Engineering, Texas A&M University, College Station, Texas 77843, United States; Department of Materials Science and Engineering, Texas A&M University, College Station, Texas 77843, United States; oorcid.org/0000-0002-2613-6016; Email: Jodie.Lutkenhaus@tamu.edu

#### **Authors**

Ian J. Echols – Artie McFerrin Department of Chemical Engineering, Texas A&M University, College Station, Texas 77843, United States

Hyosung An − Artie McFerrin Department of Chemical Engineering, Texas A&M University, College Station, Texas 77843, United States; orcid.org/0000-0001-8710-1012

Junyeong Yun – Artie McFerrin Department of Chemical Engineering, Texas A&M University, College Station, Texas 77843, United States

Kasturi T. Sarang — Artie McFerrin Department of Chemical Engineering, Texas A&M University, College Station, Texas 77843, United States

Ju-Hyun Oh – Artie McFerrin Department of Chemical Engineering, Texas A&M University, College Station, Texas 77843, United States

Touseef Habib — Artie McFerrin Department of Chemical Engineering, Texas A&M University, College Station, Texas 77843, United States

Xiaofei Zhao — Artie McFerrin Department of Chemical Engineering, Texas A&M University, College Station, Texas 77843, United States; orcid.org/0000-0002-0593-8490

Huaixuan Cao – Artie McFerrin Department of Chemical Engineering, Texas A&M University, College Station, Texas 77843, United States

Dustin E. Holta – Department of Materials Science and Engineering, Texas A&M University, College Station, Texas 77843, United States

Miladin Radovic — Department of Materials Science and Engineering, Texas A&M University, College Station, Texas 77843, United States

Micah J. Green — Artie McFerrin Department of Chemical Engineering, Texas A&M University, College Station, Texas 77843, United States; Department of Materials Science and Engineering, Texas A&M University, College Station, Texas 77843, United States; orcid.org/0000-0001-5691-0861

Complete contact information is available at: https://pubs.acs.org/10.1021/acs.langmuir.1c01904

#### Notes

The authors declare no competing financial interest.

#### ACKNOWLEDGMENTS

This work was supported by the US National Science Foundation (grant CMMI-1760859). Use of the TAMU Materials and Characterization Facility is acknowledged.

## REFERENCES

- (1) Decher, G.; Lehr, B.; Lowack, K.; Lvov, Y.; Schmitt, J. New nanocomposite films for biosensors: layer-by-layer adsorbed films of polyelectrolytes, proteins or DNA. *Biosens. Bioelectron.* **1994**, *9*, 677–684.
- (2) An, H.; Habib, T.; Shah, S.; Gao, H.; Radovic, M.; Green, M. J.; Lutkenhaus, J. L. Surface-agnostic highly stretchable and bendable conductive MXene multilayers. *Sci. Adv.* **2018**, *4*, eaaq0118.
- (3) Natu, V.; Sokol, M.; Verger, L.; Barsoum, M. W. Effect of Edge Charges on Stability and Aggregation of  ${\rm Ti}_3{\rm C}_2{\rm T}_z$  MXene Colloidal Suspensions. *J. Phys. Chem. C* **2018**, *122*, 27745–27753.
- (4) Echols, I. J.; An, H.; Zhao, X.; Prehn, E. M.; Tan, Z.; Radovic, M.; Green, M. J.; Lutkenhaus, J. L. pH-Response of polycation/ $Ti_3C_2T_x$  MXene layer-by-layer assemblies for use as resistive sensors. *Mol. Syst. Des. Eng.* **2020**, *5*, 366–375.
- (5) An, H.; Habib, T.; Shah, S.; Gao, H.; Patel, A.; Echols, I.; Zhao, X.; Radovic, M.; Green, M. J.; Lutkenhaus, J. L. Water Sorption in MXene/Polyelectrolyte Multilayers for Ultrafast Humidity Sensing. ACS Appl. Nano. Mater. 2019, 2, 948–955.
- (6) Weng, G.-M.; Li, J.; Alhabeb, M.; Karpovich, C.; Wang, H.; Lipton, J.; Maleski, K.; Kong, J.; Shaulsky, E.; Elimelech, M.; Gogotsi, Y.; Taylor, A. D. Layer-by-Layer Assembly of Cross-Functional Semitransparent MXene-Carbon Nanotubes Composite Films for Next-Generation Electromagnetic Interference Shielding. *Adv. Funct. Mater.* 2018, 28, 1803360.
- (7) Zhou, Z.; Panatdasirisuk, W.; Mathis, T. S.; Anasori, B.; Lu, C.; Zhang, X.; Liao, Z.; Gogotsi, Y.; Yang, S. Layer-by-layer assembly of MXene and carbon nanotubes on electrospun polymer films for flexible energy storage. *Nanoscale* **2018**, *10*, 6005–6013.
- (8) Tian, W.; VahidMohammadi, A.; Wang, Z.; Ouyang, L.; Beidaghi, M.; Hamedi, M. M. Layer-by-layer self-assembly of pillared two-dimensional multilayers. *Nat. Commun.* **2019**, *10*, 2558.
- (9) Li, K.; Jiao, T.; Xing, R.; Zou, G.; Zhao, Q.; Zhou, J.; Zhang, L.; Peng, Q. Fabrication of hierarchical MXene-based AuNPs-containing core—shell nanocomposites for high efficient catalysts. *Green Energy Environ.* **2018**, 3, 147–155.
- (10) Li, K.; Zou, G.; Jiao, T.; Xing, R.; Zhang, L.; Zhou, J.; Zhang, Q.; Peng, Q. Self-assembled MXene-based nanocomposites via layer-by-layer strategy for elevated adsorption capacities. *Colloids Surf., A* **2018**, 553, 105–113.
- (11) Naguib, M.; Kurtoglu, M.; Presser, V.; Lu, J.; Niu, J.; Heon, M.; Hultman, L.; Gogotsi, Y.; Barsoum, M. W. Two-Dimensional Nanocrystals Produced by Exfoliation of Ti<sub>3</sub>AlC<sub>2</sub>. *Adv. Mater.* **2011**, 23, 4248–4253.
- (12) Ling, Z.; Ren, C. E.; Zhao, M.-Q.; Yang, J.; Giammarco, J. M.; Qiu, J.; Barsoum, M. W.; Gogotsi, Y. Flexible and conductive MXene films and nanocomposites with high capacitance. *Proc. Natl. Acad. Sci.* **2014**, *111*, 16676–16681.
- (13) Anasori, B.; Lukatskaya, M. R.; Gogotsi, Y. 2D metal carbides and nitrides (MXenes) for energy storage. *Nat. Rev. Mater.* **2017**, *2*, 16098.
- (14) Han, M.; Shuck, C. E.; Rakhmanov, R.; Parchment, D.; Anasori, B.; Koo, C. M.; Friedman, G.; Gogotsi, Y. Beyond Ti<sub>3</sub>C<sub>2</sub>T<sub>x</sub>: MXenes for Electromagnetic Interference Shielding. *ACS Nano* **2020**, *14*, 5008–5016.

- (15) Yuan, W.; Yang, K.; Peng, H.; Li, F.; Yin, F. A flexible VOCs sensor based on a 3D Mxene framework with a high sensing performance. *J. Mater. Chem. A* **2018**, *6*, 18116–18124.
- (16) Hong, W.; Wyatt, B. C.; Nemani, S. K.; Anasori, B. Double transition-metal MXenes: Atomistic design of two-dimensional carbides and nitrides. *MRS Bull.* **2020**, *45*, 850–861.
- (17) Halim, J.; Persson, I.; Moon, E. J.; Kühne, P.; Darakchieva, V.; Persson, P. O. Å.; Eklund, P.; Rosen, J.; Barsoum, M. W. Electronic and optical characterization of 2D Ti<sub>2</sub>C and Nb<sub>2</sub>C (MXene) thin films. *J. Phys.: Condens. Matter* **2019**, *31*, 165301.
- (18) Halim, J.; Cook, K. M.; Naguib, M.; Eklund, P.; Gogotsi, Y.; Rosen, J.; Barsoum, M. W. X-ray photoelectron spectroscopy of select multi-layered transition metal carbides (MXenes). *ApSS* **2016**, *362*, 406–417.
- (19) Xie, Y.; Kent, P. R. C. Hybrid density functional study of structural and electronic properties of functionalized  $Ti_{n+1} X_n$  (X = C, N) monolayers. *Phys. Rev.B* **2013**, 87, 235441.
- (20) Zhao, X.; Vashisth, A.; Blivin, J. W.; Tan, Z.; Holta, D. E.; Kotasthane, V.; Shah, S. A.; Habib, T.; Liu, S.; Lutkenhaus, J. L.; Radovic, M.; Green, M. J. pH, Nanosheet Concentration, and Antioxidant Affect the Oxidation of Ti<sub>3</sub>C<sub>2</sub>T<sub>x</sub> and Ti<sub>2</sub>CT<sub>x</sub> MXene Dispersions. *Adv. Mater. Interfaces* **2020**, *7*, 2000845.
- (21) Echols, I. J.; Holta, D. E.; Kotasthane, V. S.; Tan, Z.; Radovic, M.; Lutkenhaus, J. L.; Green, M. J. Oxidative Stability of  $Nb_{n+1}C_nT_z$  MXenes. *J. Phys. Chem. C* **2021**, *125*, 13990–13996.
- (22) Zhao, X.; Vashisth, A.; Prehn, E.; Sun, W.; Shah, S. A.; Habib, T.; Chen, Y.; Tan, Z.; Lutkenhaus, J. L.; Radovic, M.; Green, M. J.; et al. *Matter* **2019**, *1*, 513–526.
- (23) Nama Manjunatha, K.; Paul, S. Investigation of optical properties of nickel oxide thin films deposited on different substrates. *Appl. Surf. Sci.* **2015**, 352, 10–15.
- (24) Ying, G.; Kota, S.; Dillon, A. D.; Fafarman, A. T.; Barsoum, M. W. Conductive transparent  $V_2CT_x$  (MXene) films. *FlatChem* **2018**, 8, 25–30.
- (25) Viezbicke, B. D.; Patel, S.; Davis, B. E.; Birnie, D. P., III Evaluation of the Tauc method for optical absorption edge determination: ZnO thin films as a model system. *Phys. Status Solidi B* **2015**, 252, 1700–1710.
- (26) Djire, A.; Zhang, H.; Liu, J.; Miller, E. M.; Neale, N. R. Electrocatalytic and Optoelectronic Characteristics of the Two-Dimensional Titanium Nitride  ${\rm Ti}_4{\rm N}_3{\rm T}_x$  MXene. ACS Appl. Mater. Interfaces 2019, 11, 11812–11823.
- (27) Elements, A. *Titanium Carbide Ti3C2*. https://www.americanelements.com/titanium-carbide-ti3c2-12363-89-2 (accessed July 7, 2021).
- (28) Elements, A. *Niobium Carbide Nb2C*. https://www.americanelements.com/niobium-carbide-nb2c-12011-99-3 (accessed July 7, 2021).
- (29) Elements, A. *Titanium Carbide Ti2C*. https://www.americanelements.com/titanium-carbide-ti2c-12316-56-2 (accessed July 7, 2021).
- (30) Lee, S. W.; Kim, B.-S.; Chen, S.; Shao-Horn, Y.; Hammond, P. T. Layer-by-Layer Assembly of All Carbon Nanotube Ultrathin Films for Electrochemical Applications. *J. Am. Chem. Soc.* **2009**, *131*, 671–679.
- (31) Doo, S.; Chae, A.; Kim, D.; Oh, T.; Ko, T. Y.; Kim, S. J.; Koh, D.-Y.; Koo, C. M. Mechanism and Kinetics of Oxidation Reaction of Aqueous  ${\rm Ti}_3{\rm C}_2{\rm T}_x$  Suspensions at Different pHs and Temperatures. ACS Appl. Mater. Interfaces 2021, 13, 22855–22865.
- (32) Song, Y.; Xu, Y.; Guo, Q.; Hua, Z.; Yin, F.; Yuan, W. MXene-Derived  ${\rm TiO_2}$  Nanoparticles Intercalating between RGO Nanosheets: An Assembly for Highly Sensitive Gas Detection. *ACS Appl. Mater. Interfaces* **2021**, *13*, 39772–39780.
- (33) Alonso, T.; Irigoyen, J.; Iturri, J. J.; larena, I. L.; Moya, S. E.; Larena, I. L.; Moya, S. E. Study of the multilayer assembly and complex formation of poly(diallyldimethylammonium chloride) (PDADMAC) and poly(acrylic acid) (PAA) as a function of pH. Soft Matter 2013, 9, 1920–1928.

- (34) Yang, Y.; Umrao, S.; Lai, S.; Lee, S. Large-Area Highly Conductive Transparent Two-Dimensional Ti<sub>2</sub>CT<sub>x</sub> Film. *J. Phys. Chem. Lett.* **2017**, *8*, 859–865.
- (35) Lin, H.; Gao, S.; Dai, C.; Chen, Y.; Shi, J. A Two-Dimensional Biodegradable Niobium Carbide (MXene) for Photothermal Tumor Eradication in NIR-I and NIR-II Biowindows. *J. Am. Chem. Soc.* **2017**, 139, 16235–16247.
- (36) Dillon, A. D.; Ghidiu, M. J.; Krick, A. L.; Griggs, J.; May, S. J.; Gogotsi, Y.; Barsoum, M. W.; Fafarman, A. T. Highly Conductive Optical Quality Solution-Processed Films of 2D Titanium Carbide. *Adv. Funct. Mater.* **2016**, *26*, 4162–4168.
- (37) Mariano, M.; Mashtalir, O.; Antonio, F. Q.; Ryu, W.-H.; Deng, B.; Xia, F.; Gogotsi, Y.; Taylor, A. D. Solution-processed titanium carbide MXene films examined as highly transparent conductor. *Nanoscale* **2016**, *8*, 16371–16378.
- (38) Ying, G.; Dillon, A. D.; Fafarman, A. T.; Barsoum, M. W. Transparent, conductive solution processed spincast 2D Ti<sub>2</sub>CT<sub>x</sub> (MXene) films. *Mater. Res. Lett.* **2017**, *5*, 391–398.
- (39) Jing, Z.; Liu, J.; Li, N.; Wang, H.; Wu, K.; Cheng, Y.; Xiao, B. Electron-phonon scattering limited intrinsic electrical conductivity of metallic MXenes  $X_2$ C (X= Ti or Mo). *J. Phys. D: Appl. Phys.* **2021**, *54*, No. 015301.
- (40) Habib, T.; Zhao, X.; Shah, S. A.; Chen, Y.; Sun, W.; An, H.; Lutkenhaus, J. L.; Radovic, M.; Green, M. J. Oxidation stability of  $Ti_3C_2T_x$  MXene nanosheets in solvents and composite films. *npj* 2D *Mater. Appl.* **2019**, *3*, 8.
- (41) Zhang, C. J.; Pinilla, S.; McEvoy, N.; Cullen, C. P.; Anasori, B.; Long, E.; Park, S.-H.; Seral-Ascaso, A.; Shmeliov, A.; Krishnan, D.; Morant, C.; Liu, X.; Duesberg, G. S.; Gogotsi, Y.; Nicolosi, V. Oxidation Stability of Colloidal Two-Dimensional Titanium Carbides (MXenes). *Chem. Mater.* **2017**, *29*, 4848–4856.
- (42) Han, M.; Maleski, K.; Shuck, C. E.; Yang, Y.; Glazar, J. T.; Foucher, A. C.; Hantanasirisakul, K.; Sarycheva, A.; Frey, N. C.; May, S. J.; Shenoy, V. B.; Stach, E. A.; Gogotsi, Y. Tailoring Electronic and Optical Properties of MXenes through Forming Solid Solutions. *J. Am. Chem. Soc.* **2020**, *142*, 19110–19118.
- (43) Velusamy, D. B.; El-Demellawi, J. K.; El-Zohry, A. M.; Giugni, A.; Lopatin, S.; Hedhili, M. N.; Mansour, A. E.; Fabrizio, E. D.; Mohammed, O. F.; Alshareef, H. N. MXenes for Plasmonic Photodetection. *Adv. Mater.* **2019**, *31*, 1807658.
- (44) Wu, Y.; Wadia, C.; Ma, W.; Sadtler, B.; Alivisatos, A. P. Synthesis and Photovoltaic Application of Copper(I) Sulfide Nanocrystals. *Nano Lett.* **2008**, *8*, 2551–2555.
- (45) Zanatta, A. R. Revisiting the optical bandgap of semiconductors and the proposal of a unified methodology to its determination. *Sci. Rep.* **2019**, *9*, 11225.
- (46) Lee, S. H.; Eom, W.; Shin, H.; Ambade, R. B.; Bang, J. H.; Kim, H. W.; Han, T. H. Room-Temperature, Highly Durable  ${\rm Ti}_3{\rm C}_2{\rm T}_x$  MXene/Graphene Hybrid Fibers for NH<sub>3</sub> Gas Sensing. ACS Appl.Mater. Interfaces **2020**, 12, 10434–10442.
- (47) Din Babar, Z. U.; Fatheema, J.; Arif, N.; Anwar, M. S.; Gul, S.; Iqbal, M.; Rizwan, S. Magnetic phase transition from paramagnetic in Nb<sub>2</sub>AlC-MAX to superconductivity-like diamagnetic in Nb<sub>2</sub>C-MXene: an experimental and computational analysis. *RSC Adv.* **2020**, *10*, 25669–25678.
- (48) Tyagi, C.; Sharma, A. Tailoring the optical properties of poly(diallyl dimethyl ammonium chloride) polyelectrolyte by incorporation of 2-mercaptoethanol capped CdSe nanoparticles. *J. Phys. D: Appl. Phys.* **2016**, *49*, 405301.
- (49) Natu, V.; Hart, J. L.; Sokol, M.; Chiang, H.; Taheri, M. L.; Barsoum, M. W. Edge Capping of 2D-MXene Sheets with Polyanionic Salts To Mitigate Oxidation in Aqueous Colloidal Suspensions. *Angew. Chem., Int. Ed.* **2019**, *58*, 12655–12660.
- (50) Lotfi, R.; Naguib, M.; Yilmaz, D. E.; Nanda, J.; van Duin, A. C. T. A comparative study on the oxidation of two-dimensional  $\mathrm{Ti}_3\mathrm{C}_2$  MXene structures in different environments. *J. Mater. Chem. A* **2018**, *6*, 12733–12743.
- (51) Lipatov, A.; Alhabeb, M.; Lukatskaya, M. R.; Boson, A.; Gogotsi, Y.; Sinitskii, A. Effect of Synthesis on Quality, Electronic

- Properties and Environmental Stability of Individual Monolayer Ti<sub>3</sub>C<sub>2</sub> MXene Flakes. *Adv. Electron. Mater.* **2016**, 2, 1600255.
- (52) Lee, Y.; Kim, S. J.; Kim, Y.-J.; Lim, Y.; Chae, Y.; Lee, B.-J.; Kim, Y.-T.; Han, H.; Gogotsi, Y.; Ahn, C. W. Oxidation-resistant titanium carbide MXene films. *J. Mater. Chem. A* **2020**, *8*, 573–581.
- (53) Zhao, X.; Holta, D. E.; Tan, Z.; Oh, J.-H.; Echols, I. J.; Anas, M.; Cao, H.; Lutkenhaus, J. L.; Radovic, M.; Green, M. J. Annealed  $Ti_3C_2T_z$  MXene Films for Oxidation-Resistant Functional Coatings. *ACS Appl. Nano. Mater.* **2020**, *3*, 10578–10585.
- (54) Fu, Z. H.; Zhang, Q. F.; Legut, D.; Si, C.; Germann, T. C.; Lookman, T.; Du, S. Y.; Francisco, J. S.; Zhang, R. F. Stabilization and strengthening effects of functional groups in two-dimensional titanium carbide. *Phys. Rev. B* **2016**, *94*, 104103.
- (55) Huang, S.; Mochalin, V. N. Hydrolysis of 2D Transition-Metal Carbides (MXenes) in Colloidal Solutions. *Inorg. Chem.* **2019**, *58*, 1958–1966.
- (56) Hanlon, D.; Backes, C.; Doherty, E.; Cucinotta, C. S.; Berner, N. C.; Boland, C.; Lee, K.; Harvey, A.; Lynch, P.; Gholamvand, Z.; Zhang, S.; Wang, K.; Moynihan, G.; Pokle, A.; Ramasse, Q. M.; McEvoy, N.; Blau, W. J.; Wang, J.; Abellan, G.; Hauke, F.; Hirsch, A.; Sanvito, S.; O'Regan, D. D.; Duesberg, G. S.; Nicolosi, V.; Coleman, J. N. Liquid exfoliation of solvent-stabilized few-layer black phosphorus for applications beyond electronics. *Nat. Commun.* **2015**, *6*, 8563.
- (57) Iqbal, A.; Hong, J.; Ko, T. Y.; Koo, C. M. Improving oxidation stability of 2D MXenes: synthesis, storage media, and conditions. *Nano Convergence* **2021**, *8*, 9.
- (58) Nunes, B. N.; Lopes, O. F.; Patrocinio, A. O. T.; Bahnemann, D. W. Recent Advances in Niobium-Based Materials for Photocatalytic Solar Fuel Production. *Catalysts* **2020**, *10*, 126.
- (59) Li, N.; Jiang, Y.; Zhou, C.; Xiao, Y.; Meng, B.; Wang, Z.; Huang, D.; Xing, C.; Peng, Z. High-Performance Humidity Sensor Based on Urchin-Like Composite of Ti<sub>3</sub>C<sub>2</sub> MXene-Derived TiO<sub>2</sub> Nanowires. *ACS Appl. Mater. Interfaces* **2019**, *11*, 38116–38125.
- (60) Hou, L.; Johnson, J. A.; Wang, S. Radio frequency heating for postharvest control of pests in agricultural products: A review. *Postharvest Biol. Technol.* **2016**, *113*, 106–118.
- (61) Gerringer, J. C.; Moran, A. G.; Habib, T.; Pospisil, M. J.; Oh, J. H.; Teipel, B. R.; Green, M. J. Radio Frequency Heating of Laser-Induced Graphene on Polymer Surfaces for Rapid Welding. *ACS Appl. Nano. Mater.* **2019**, *2*, 7032–7042.
- (62) Piyasena, P.; Dussault, C.; Koutchma, T.; Ramaswamy, H. S.; Awuah, G. B. Radio Frequency Heating of Foods: Principles, Applications and Related Properties—A Review. *Crit. Rev. Food Sci. Nutr.* **2003**, *43*, 587–606.
- (63) Tiwari, G.; Wang, S.; Tang, J.; Birla, S. L. Computer simulation model development and validation for radio frequency (RF) heating of dry food materials. *J. Food Eng.* **2011**, *105*, 48–55.
- (64) Tezel, G. B.; Sarmah, A.; Desai, S.; Vashisth, A.; Green, M. J. Kinetics of carbon nanotube-loaded epoxy curing: Rheometry, differential scanning calorimetry, and radio frequency heating. *Carbon* **2021**, *175*, 1–10.
- (65) Habib, T.; Patil, N.; Zhao, X.; Prehn, E.; Anas, M.; Lutkenhaus, J. L.; Radovic, M.; Green, M. J. Heating of  ${\rm Ti_3C_2T_x}$  MXene/polymer composites in response to Radio Frequency fields. *Sci. Rep.* **2019**, *9*, 16489
- (66) Shahzad, F.; Alhabeb, M.; Hatter, C. B.; Anasori, B.; Man Hong, S.; Koo, C. M.; Gogotsi, Y. Electromagnetic interference shielding with 2D transition metal carbides (MXenes). *Science* **2016**, 353, 1137–1140.
- (67) Wang, H.; Peng, R.; Hood, Z. D.; Naguib, M.; Adhikari, S. P.; Wu, Z. Titania Composites with 2 D Transition Metal Carbides as Photocatalysts for Hydrogen Production under Visible-Light Irradiation. *ChemSusChem* **2016**, *9*, 1490–1497.
- (68) Zhou, X.; Guo, Y.; Wang, D.; Xu, Q. Nano friction and adhesion properties on  $Ti_3C_2$  and  $Nb_2C$  MXene studied by AFM. *Tribol. Int.* **2021**, *153*, 106646.
- (69) Gu, M.; Dai, Z.; Yan, X.; Ma, J.; Niu, Y.; Lan, W.; Wang, X.; Xu, Q. Comparison of toxicity of  $Ti_3C_2$  and  $Nb_2C$  Mxene quantum dots

(QDs) to human umbilical vein endothelial cells. J. Appl. Toxicol.

2021, 41, 745–754.

(70) Liu, F.; Zhou, A.; Chen, J.; Jia, J.; Zhou, W.; Wang, L.; Hu, Q. Preparation of Ti<sub>3</sub>C<sub>2</sub> and Ti<sub>2</sub>C MXenes by fluoride salts etching and methane adsorptive properties. *Appl. Surf. Sci.* 2017, 416, 781–789.